Design, imaging and performance of 3D printed open-cell architectures for porous electrodes: Quantification of surface area and permeability

N. Kaishubayeva,[†] C. Ponce de León, F.C. Walsh, L.F. Arenas[+,‡,*]

Electrochemical Engineering Laboratory, Faculty of Engineering and the Environment,

University of Southampton, Southampton, SO17 1BJ, UK.

*Author for correspondence; L.F. Arenas, lfam1c17@soton.ac.uk, +52 5521855366

Abstract

Background: The development of new open-cell porous electrodes for electrochemical flow cells and reactors is demonstrated through the application of 3D printing. The properties of diverse architectures were investigated, including rectangular, circular, hexagonal and triangular cells with linear porosity grades of 10, 20 and 30 pores per inch. Specimens were digitally designed, then 3D printed in stainless steel via selective laser melting. After being examined using scanning electron microscopy, they were characterised in terms of volumetric surface area and porosity with the aid of X-ray computed tomography. Pressure drop measurements were performed over a range of mean linear velocity and Reynolds number, allowing the estimation of Darcy's friction factor and permeability.

Results: Volumetric surface area estimated from tomography scans was up to 36% higher than the nominal values due to surface roughness and post-processing algorithms. In contrast, volumetric porosity obtained by tomography agreed fully with measured values. Triangular architectures afforded additional surface area both digitally and according to tomography. The largest pressure drop was found in circular materials, the triangular ones showing the lowest. The 20 ppi triangular architecture had a volumetric surface area of approximately 44.5 cm^{-1} and a permeability of 2.31×10^{-5} cm^2.

Conclusion: Triangular architectures were preferred due to their favourable combination of high surface area and high permeability with low mass and reduced digital complexity. This provides a strategy to initiate the optimization of 3D printed porous electrodes for electrochemical flow cells and reactors in novel and niche applications.

[†] Present address: Nur-Sultan, Kazakhstan.

[‡] Present address: Independent consultant. Saltillo, Mexico.

[+] Society of Chemical Industry active member.

Symbols

A	Surface area	cm^2
A_e	Volumetric surface area	cm^{-1}
A_{sv}	Surface area per unit volume of solid material	cm^{-1}
D	Diameter of porous electrode	cm
d	Hydraulic channel diameter	cm
e	Empirical coefficient in Eq. (5)	Pa
F	Faraday constant	C mol^{-1}
f_D	Darcy's friction factor	dimensionless
H	Height of porous electrode	cm
h	Empirical coefficient in Eq. (5)	dimensionless
I_L	Limiting current	A
K_D	Darcy's permeability	cm^2
k_m	Mass transfer coefficient	cm s^{-1}
L	Length of porous electrode in the direction of flow	cm
m	Mass	g
P	Pressure	Pa
Q	Volumetric flow rate	cm^3 s^{-1}
Re	Reynolds number	dimensionless
V_{bulk}	Bulk volume of the electrode	cm^3
V_e	Overall volume of the porous electrode	cm^3
V_{solid}	Volume of solid metal in the electrode	cm^3
v	Mean linear velocity of fluid	cm s^{-1}
W	Width of porous electrode	cm

Greek symbols

ΔP	Pressure drop	Pa
ε	Volumetric porosity	dimensionless

μ	Dynamic viscosity of fluid	g cm^{-1} s^{-1}
ρ	Density	g cm^{-3}

Abbreviations

3D	Three dimensional
CAD	Computer-aided design
CT	X-ray computed tomography
ppi	Pores per linear inch (porosity grade)
ROI	Region of interest
RTD	Residence time distribution
RVC	Reticulated vitreous carbon
SEM	Scanning electron microscopy
SLM	Selective laser melting
TP	Turbulence promoter

Introduction

Interest in innovative 3D printed electrochemical devices continues to grow.[1,2] One of the most important and promising applications is the development of tailored electrochemical flow reactors with enhanced efficiency for electrochemical processing and energy storage and conversion.[3,4] 3D printing already offers the possibility of manufacturing fast prototypes[5] and working models of electrochemical flow reactors[6] and electrolysers,[7] enabling their design through a recently proposed cycle of conceptualization, simulation, rapid prototyping and experimental validation.[8,9] However, it is also important to adequately assess the characteristics of electrodes produced by 3D printing in order to predict their performance realistically and to enable the design of improved electrochemical reactors.

A growing number of 3D printed architectures are based on periodic cellular materials for use as porous electrodes in electrochemical technologies.[10,11] Such electrodes increase the productivity of electrochemical reactors by providing extended active surface area and enhancing mass transfer of reactants compared to planar electrodes.[12] Ideally, porous electrode materials should have good electrical conductivity, high volumetric surface area and high hydraulic permeability,[13] leading to more efficient, compact reactors. The electrode structure can then be modified using a wide diversity of catalysts and hierarchical structures, adding functionality and selectivity.[14,15] 3D printing can provide control over pore size and shape, distance between pores, volumetric porosity and surface area of the porous structures within the manufacturing resolution. Such advances could find novel or niche applications for 3D printed electrodes in water treatment,[16,17] electrosynthesis,[18,19] environmental remediation,[20,21] and energy storage.[22,23]

In the case of 3D printed metallic electrodes,[15] the technique chosen in this contribution creates tailored architectures by layer-by-layer deposition of a precursor powder through selective laser melting (SLM).[24] Compared to other laser-based techniques, SLM results in better surface morphology, homogeneity and mechanical properties. It permits the production of components not only in ferrous alloys but also in titanium, aluminium and copper.[24] The potential for this concept in electrochemical flow cells has been demonstrated by 3D printed stainless steel electrodes coated with nickel[3] and MoS_2[7] and by 3D printed titanium electrodes coated with TiO_2[25] and platinum.[26] SLM has also been applied to produce helical electrodes,[27] moulds for sintered electrodes[28] as well as static cells for sensors[29] and oxygen evolution.[30]

The analysis of 3D printed porous electrodes can be carried out by X-ray computed tomography (CT) in order to estimate or validate their volumetric porosity, solid volume, physical surface area and derived parameters.[31] These characteristics are essential to assess their performance and to the calculation or simulation of their hydrodynamic, ohmic and kinetic behaviour.[32] The physical surface area of these materials and its comparison to active electrochemical surface area is particularly important in electrochemical studies.[33,34] Examples involving conventional porous electrodes by CT include the tortuosity of carbon felt,[35] the surface area of reticulated vitreous carbon (RVC)[31] and the distribution of metal deposits such as copper and cadmium[36] or platinum.[37,38] Related examples of the analysis of inert porous materials by CT include the determination of pore diameter distribution in $SiC-Al_2O_3$ foams[39] and the study of porosity and tortuosity in SiC foams.[40] Similar structural and parametrical analysis would certainly be of

interest in non-electrochemical 3D printed flow reactors, such as those recently proposed for the enhancement of heterogeneous reactions and separation processes.[41]

Following the characterization of the material, the performance of a porous electrode in an electrochemical flow reactor can be quantified by the volumetric mass transfer coefficient, k_mA_e, and its relationship to the pressure drop, ΔP, which is caused by frictional losses as the electrolyte flows through the porous structure.[3,42,43] The first is strongly related to the limiting current density and the minimization of overpotentials.[12] The latter depends on the permeability of the material which affects pumping energy demand and energy efficiency.[44] A low pressure drop also facilitates the assembly and operation of leak-free reactors. Electrodes having high volumetric surface area and high permeability are required for an energy efficient electrochemical process. A comparative study of porous electrode architectures can be initiated by seeking such characteristics, before progressing to electrochemical aspects.

After introducing 3D printed porous electrodes for electrochemical flow reactors[3] and applying CT to the analysis of the surface area of porous electrodes,[31] we now turn our attention to the development of diverse 3D printed porous architectures for use in electrochemical flow reactors. This approach is an example of a 'virtuous cycle' in which a rational development for porous electrodes, based on the digital design of tailored structures, is followed by their manufacture, subsequent imaging and analysis of their physical properties then the evaluation of their performance.[8,9] See Figure 1. Up to now, attention has been focused on the achievement of smaller pore sizes or on the increase of mass transfer, neglecting the parameters of surface area (which is

directly linked to the electrochemical performance) and hydraulic permeability (which is of utmost importance in a practical flow device.) The novelty of this work lies in the methodology for selecting a 3D printed electrode architecture. We have aimed for maximum surface area and high hydrodynamic permeably, an important step towards the development of advanced electrode materials. Work in progress will utilise the results of this study in the assessment of the electrochemical performance and application of the 3D printed electrodes under mass transfer-controlled conditions.

Theoretical considerations

Surface area

The volumetric surface area, A_e, is an important property of a porous electrode material and is the ratio of its total surface area, A, to its volume V_R (in a specimen or inside an electrochemical reactor):

$$A_e = \frac{A}{V_R} \tag{1}$$

A_e, can then be used to rationalize the performance factor $k_m A_e$ via the estimation of a limiting current, I_L, or mass transfer coefficient, k_m, during electrochemical characterization of the material.[34,45,46]

The electrode area per unit solid volume, A_{sv}, is related to A_e and the volumetric porosity of the material, ε :[47]

$$A_{sv} = \frac{A_e}{(1-\varepsilon)} \qquad (2)$$

A_{sv} can also be determined using the Ergun equation in the case of materials with relatively small pore sizes,[39,48] facilitating comparison with other porous electrodes. The value of A_{sv} is particularly useful as an indicator of how well a porous body can maximise its surface area. A similar parameter is the specific surface area, which relates surface area and mass of material.

Pressure drop

Regarding pressure drop through the porous electrodes, a normalization is useful, in terms of the fluid flow regime, to enable comparisons. A simple approach can consider the mean linear velocity of the fluid, v as it passes through the porous material. It is given by the expression:[49]

$$v = \frac{Q}{\varepsilon A_x} \qquad (3)$$

where Q is volumetric flow rate and A_x is the cross-sectional area of the porous material.

Classically, a dimensionless Reynolds number, $Re,$ considering the hydraulic diameter of the flow channel/tube, $d,$ as characteristic length can be used to define the fluid flow within the porous material in terms of the properties of the fluid:

$$Re = \frac{\rho v d}{\mu} \qquad (4)$$

where ρ is density and μ is dynamic viscosity. The experimental value of ΔP can be conveniently fitted to an empirical power law involving Re:[50]

$$\Delta P = eRe^h \tag{5}$$

where e and h are empirical constants; their values define this relationship, which is specific to each porous material.

ΔP can be used to calculate Darcy's friction factor, f_D, as an indicator of the intensity of frictional losses. This friction factor can be plotted as a function of v or Re allowing a comparison of different porous media:

$$f_D = \frac{2\Delta P d}{L\rho v^2} \tag{6}$$

where L is the length of the porous material experiencing the flow. Darcy's friction factor, f_D has been employed to characterize rough electrodes,[51] mesh spacers [52,53] and porous electrodes.[42,54]

Similarly, Darcy's permeability, K_D can be used to characterise the influence of electrode geometry on the fluid flow.[55] From Darcy's law, this property defines how fast fluid passes through a volume of porous material per unit of differential pressure and is an indicator of how well the pores are interconnected.[48] It is calculated from the expression:

$$K_D = \frac{v\mu L}{\Delta P} \tag{7}$$

K_D has been used to describe the suitability of electrode materials in electrochemical reactors,[56] for instance in redox flow batteries.[54,57] K_D is also important in the study of hydraulic properties of 3D printed replicas of open cell foams.[58]

Experimental

Design of the porous materials

Nine porous electrode architectures were designed using SolidWorks CAD suite (Dassault Systèmes SA, France). The open-cell pores were designed in four geometrical shapes: rectangular, circular, hexagonal and triangular. Drawings for each architecture are found in the Supplementary Material; Figures S1 to S4. The distances between the two closest edges of neighbouring pores were selected so as to form 10 ppi (linear pores per inch), 20 ppi and 30 ppi structures, being limited by computer processing power; the finer the structure, the longer time to manipulate a model. Figure 2 presents CAD examples of each geometrical shape for the 10 ppi porosity grade only, for clarity. Cross-sectional views are found in the Supplementary Material; Figures S5. All the architectures were envisaged and printed as cylindrical specimens with a diameter of 30 mm and a height of 20 mm. The nine different electrode architectures can be seen in Figure 3. The arrangement of the pores was such that they formed rectilinear grids in the horizontal direction which were staggered in the vertical direction. The characteristic lengths of the void, interconnected cells ranged from 0.7 mm to 2.6 mm. Table 1 provides a list of their nominal characteristic lengths, linear and volumetric porosity and surface areas according to the CAD program.

3D printing of porous materials

The complex porous geometries, which would have been very problematic to manufacture using traditional machining methods, were printed layer-by-layer using a M2 Cusing (ConceptLaser GmbH, Germany) SLM metal printer with a maximum resolution of 20 micrometres and a power of 200 W under a N_2 gas environment. The precursor powder was a 316L (CL20 ES) austenitic stainless-steel (Fe base containing 17.5% Cr, 11.5% Ni, 2.3% Mo) with particle sizes between 20 and 40 μm in diameter. The 3D printed electrode materials are shown in the Supplementary Material; Figure S6a). The mass, diameter and height of the specimens were measured in order to determine their volumetric porosity, ε, and compare it with CAD values. Assuming that the internal microporosity of the material was negligible, ε was calculated from the expression:

$$\varepsilon = \frac{V_{bulk} - V_{solid}}{V_{bulk}} \tag{8}$$

where V_{bulk} is the bulk volume of the specimen and V_{solid} is the volume of the metal. These values were calculated using the following equations:

$$V_{bulk} = \frac{\pi}{4} D^2 H \tag{9}$$

$$V_{solid} = \frac{m}{\rho} \tag{10}$$

where D and H are the measured diameter and height of the specimen, respectively, m is the mass of the material and ρ is the density of stainless steel (7.98 g cm^{-3} for austenitic grade 316L material).[59] Mass was measured in an analytical balance (Mettler-Toledo Inc., USA) to an accuracy of ±1 mg. Dimensions of the 3D printed samples were taken with a digital calliper (Mitutoyo Corp., Japan).

SEM and CT imaging

SEM images of the 3D printed specimens were obtained at 15 kV using a JSM-6500F field emission electron microscope (Jeol Inc, USA). X-ray CT scans were performed in a modified Nikon/Xtek HMX equipment (Nikon Corp., Japan) under a peak voltage of 195 kV and a current of 115 μA. A CT rendering was constructed from 3401 projections with 2 frames per projection, each frame taking 708 ms. Shutting was enabled and a filtration of 1 mm of copper was used. The resulting isotropic resolution was 0.0187 mm per voxel. The scan time for each specimen was approximately 2.5 hours. Raw images were processed and analysed using VG Studio MAX v.2.1 (Volume Graphics GmbH, Germany). Volume and surface area were established using the 'ISO50%' threshold condition.

Pressure drop measurements

Pressure drop measurements were carried out with distilled water in a tubular, circular section flow cell with internal and external diameters of 30 mm and 40 mm, respectively. The clear acrylic polymer flow cell consisted of two threaded tube segments; see Figure S6b). The entry segment had a length of 30.0 cm, which is ten times larger than the internal diameter, to achieve a fully developed flow in the test section.[60] The outlet segment had a length of 10.0 cm and part of it had a wider internal diameter (3.02 cm) to hold the electrode samples. In order to prevent any bypassing of flow, waterproof adhesive tape was placed between the samples and the tube by compression; see Figure S6c). Pressure drop was measured with a HT-1890 digital manometer (Risepro, China) at pressure taps drilled in the flow cell as close to the porous material as the arrangement allowed,

using two polypropylene tubes (2 mm internal diameter) sealed with epoxy resin; see Figure S6d). During the experiments, the flow cell was mounted horizontally, having first removed air bubbles from it in the vertical position. Three sets of measurements at different volumetric flow rates were taken for each material and an average value was reported. A fluid (water) density of 1 g cm^{-3} and a dynamic viscosity of 8.9 × 10^{-4} Pa s at 25 ºC were used in Reynolds number calculations. The flow cell was connected to a NEMP50/7 magnetically coupled centrifugal pump (Totton Pumps, UK) through polypropylene tubing, providing volumetric flow rates up to 440 litres per hour. The temperature was maintained at 25±1 ºC by a thermostatic water bath (Grant Instruments Ltd, UK).

Results and Discussion

SEM and CT characterisation

SEM images of the top faces of the 3D printed porous architectures are shown in Figure 3. Layers of stainless steel powder melted by laser and fused during SLM are clearly visible. As expected, some distortion and surface roughness are found in the structure due to the manufacture method, especially with decreasing pore size. Nodules < 0.1 mm in size protrude from the sides and small pores can be observed at the junction of struts. Such deviations result in slightly different volume and surface area from the designed geometrical shapes. A larger surface area can be expected to increase the electrochemical performance while surface roughness can enhance mixing and mass transfer, albeit by promoting frictional losses in the fluid.

CT scans of selected porous structures were also obtained. As an example, Figures 4a), c), e) and g) depict the volume occupied by 3D printed specimens (20 ppi grade) according to the 'ISO50%' thresholding standard within cylindrical regions of interest (ROI) of 10 mm diameter and 5 mm height. Several properties were determined from post-processing these scans, *vide infra*. CT also provided cross-sectional cuts of the specimens, allowing to observe the quality of the internal scaffold of the specimens. As shown in Figures 4b), d), f) and h), cross-sectional CT images indicate that the manufacture technique can produce some distortions in the regularity of the structure. This is attributable to the tolerances in the laser movement relative to the position of the specimen, temperature changes and interruptions during the process. Figure 4f) also shows in particular that horizontal components of the pores bent downwards as layers of molten metal powder were applied. This effect is less evident in the samples with smaller sizes of pores. Because uniform pore distribution was proved to increase efficiency in porous electrodes under possible mass transfer limitations,[61] further control of the porous structure may be achieved by using a higher resolution, slower speed or more rigid support during printing.

Table 2 shows the measured mass, diameter and height of the 3D printed porous materials. The diameter and height of the specimens deviated by no more than 2.3% from the designed values. The actual volumetric porosity of the specimens, given reliably by their mass and density, was lower than that of the digital designs. For 10 ppi grade materials, the difference was near 5%, whereas for 20 ppi and 30 ppi grade materials it rose to 20% and 30%, respectively. This is the result of the manufacturing tolerances imposed by the SLM technique. On the other hand, the porosity values determined from CT scans, see Table 2, are close to the ones calculated from direct mass measurements, with a maximum error of 3%. This implies that CT-determined porosity

values are reasonably accurate for these materials, as opposed to their nominal CAD dimensions. Indeed, in previous work on the study of RVC by CT,[62] it was found that this technique was useful in determining properties derived from a 3D volume (such as porosity), whereas those derived from 2D surfaces required *ad hoc* image post processing and calibration in order to achieve sufficient accuracy.

The estimation of the surface area of 3D printed porous materials from CT scans was also explored. As seen in Table 2, the CT values are higher than the nominal CAD values due to the roughness of the manufactured samples. In the case of the rectangular pores, the difference in the surface area increases along linear porosity grade but the opposite is true in the case of the samples with triangular pores. Given the limited number of specimens, a clear trend cannot be established in relation to surface area *vs*. porosity at this point. However, it can be safely assumed that the real surface area of these porous geometries is larger than in the CAD drawings. As mentioned above, surface area properties are less accurate than the CT-determined volumetric porosity.[31] A validation of the surface area of the 3D printed specimens as estimated by CT would require demanding work and careful consideration of the resolution and thresholding algorithms used to process the CT rendering of the specimens,[63] as it is known that the ISO50% algorithm is not always accurate.[64] These tasks are outside the scope of this work but such dependencies have been discussed in the case of RVC.[31]

The values of A_e and A_{sv} can be calculated from the surface area values for the 3D printed electrode architectures using Eqs. (1) and (2), respectively. The results are shown in Table 3. As expected,

the magnitude of both properties increases with the nominal linear porosity grade. However, when comparing the structures with the same nominal ppi, the triangular pore architecture clearly affords the largest values among the geometrical pore shapes studied. For the triangular pores at a 20 ppi pore grade $A_e = 44.49$ cm^{-1} and $A_{sv} = 211.86$ cm^{-1} from CAD values. Such values can be contrasted to those of random, open-cell electrode materials. For nickel foam, A_e ranges between 35.0 and 92.5 cm^{-1} and A_{sv} between 1400 and 3700 cm^{-1} as the porosity grade increases from 45 to 100 ppi.[47] In the case of RVC, A_e ranges between 13.5 and 67.55 cm^{-1} as the porosity grade increases from 10 to 100 ppi.[62]

A_{sv} defines how effective is a given structure to produce a surface out of solid material. An expression of this value as a function of A_e produces a characteristic relationship for a given porous material. An ideal plot of A_{sv} vs. A_e from CAD surface area values is found on Figure 5a) as a benchmark for all the architectures. There are apparent linear relationships for all the cases between 10 and 20 ppi, notably passing through the origin, as in the case of RVC between 10 and 100 ppi, which has a dimensionless slope value of approximately 25.7, as calculated from the A_e values from Friedrich et al.[65] and the ε values from Arenas et al.[31] See Figure S7 in the Supplementary Material. However, two slopes are found in the porous electrode architectures, one for the triangular geometry (4.76) and one for the other geometries (4.01). Such a high slope in the case of RVC reflects its much higher porosity, typically 0.97. The rectangular pore geometry in a 30 ppi porosity grade material did not lie on the straight line relationship, this being the only sample having that linear porosity grade. Similarly, 100 ppi RVC, the highest porosity grade, appears to deviate from linearity. Further studies could focus on the physical origin of variation the characteristics of 3D printed porous electrodes over a wide range of ppi.[40,66]

A plot of A_{sv} vs. A_e constructed from real surface area values established by CT (rather than CAD ideal values) would be useful in practice and would reveal manufacturing tolerances. However, as shown above, the surface area values established by CT are not entirely accurate in this work due to the further need for validated CT metrology of porous structures. However, a plot of A_{sv} vs. A_e can still be presented cautiously for comparison purposes. Indeed, as shown in Table 3, A_e values are up to 35% larger while A_s is underestimated with a large dispersion between 3 and 38%. The fact that CT surface area properties are not accurate for the 3D printed specimens in this work is reinforced by the fact that the linear relationship of A_{sv} vs. A_e intersects the y axis at a positive value. See Figure 5b). |Similar behaviour was observed when surface areas were calculated for RVC from CT scans with insufficient resolution in disagreement with direct methods.[31] Clearly, there are research opportunities in studying the metrology of open-cell 3D printed porous materials and improving software approaches to the computation of surface area-related characteristics.

Pressure drop

The pressure drop taking place across the 20 mm-long 3D printed porous samples is shown in Figure 6a) as a function of mean linear velocity and in Figure 6b) as a function of the channel Reynolds number (where tube diameter is the characteristic length). Following the typical behaviour, the pressure drop increased along the flow rate for all the specimens, spanning about two orders of magnitude. As expected due to their larger pore sizes, 10 ppi triangular, rectangular and hexagonal structures exhibited a relatively low pressure drop throughout the whole range of flow rate and Reynolds numbers. For the maximum common mean linear flow velocity of

approximately 14 cm s^{-1}, their values were 463.7 Pa, 670.4 Pa and 744.6 Pa, respectively. In contrast, the 10 ppi and 20 ppi circular pore geometry specimens showed the highest values due to their small pores between cells. Their corresponding values near 14 cm s^{-1} were 5.4 kPa and 8.7 kPa, respectively. The 30 ppi rectangular sample, which had the smallest pore size (0.7 mm), displayed a pressure drop of 5.88 kPa at the common linear flow velocity. Its behaviour is comparable to the circular 10 ppi structure. The observed trends dot not change in any substantial way when the Reynolds number is considered instead. As anticipated, the pressure drop was lowest for the samples having the lowest porosity grade, in accordance with other studies,[55,67,68] including experiments with 3D printed open-cell metal foams of 3.5 ppi, 4.5 ppi and 6 ppi.[69]

Although normalized parameters are studied in the next sections, it is worth contrasting these results to the pressure drop obtained at other porous materials. For instance, the pressure drop of water at a 38 mm-long, uncompressed 10 ppi aluminium foam was 200 Pa at 10 cm s^{-1},[68] a reasonably lower value in view of its 0.92 volumetric porosity. Carbon felt, a common electrode material,[70] produced a pressure drop of 60 kPa at 4 cm s^{-1} in a 12 cm long flow channel when having a with a compression ratio of 80% in 0.5 mol dm^{-3} Na$_2$SO$_4$.[71] To put this in perspective, the combined ΔP in the ElectroSynCell® pilot-scale electrochemical reactor with 60 ppi grade nickel foams at an electrolyte (0.5 mol dm^{-3} aqueous NaOH) volumetric flow rate of 132 cm^3 s^{-1} was measured at 14.4 kPa.[72]

The relationship between pressure drop and Reynolds can be described in a practical manner by a log-log plot, as shown in Figure 7. Here, the pressure drop over the 3D printed porous materials

follows a linear power law (see Eq. 5). Thus, a set of two empirical coefficients can characterize their behaviour. These values are given in Table 4, along values found in the literature for Pt/Ti felt ($\varepsilon = 0.80$), mesh ($\varepsilon = 0.71$), micromesh ($\varepsilon = 0.53$) and a polypropylene turbulence promoter (TP) mesh ($\varepsilon = 0.78$) in a rectangular flow channel,[73] the FM01-LC electrochemical reactor,[50] and a rectangular channel reactor with a small interelectrode gap.[74] It can be seen that, for these 3D printed materials, the values for the exponent h, fall between 1.16 and 1.57, the higher values corresponding to smaller pores. Consistently, a coarse mesh has a value of only 0.61. Meanwhile, a 95 mm-long Ni plate having a turbulence promoter mesh shows a similar behaviour to the stainless steel specimens. As a note, the values for e of the 3D printed porous materials are lower than unity because their ΔP *vs. Re* double logarithmic lines have negative y-values at the intercept.

Although beyond the scope of this work, it is worth mentioning that the hydrodynamic properties of porous electrodes can be implemented in the design of 3D printed structures and integrated with advanced image analysis. Examples of such an approach can be found in the field of pressure drop modelling at porous solids. For instance, periodic open-cell metallic foams were 3D printed using selective electron beam melting in order to estimate their surface area from pressure drop measurements[69] and the pressure drop at Al_2O_3 foams was modelled from structural parameters determined from magnetic resonance imaging and later determined from pressure drop studies.[55] More recently, porosity and tortuosity of SiC foams obtained from CT scans were used to predict the pressure drop across these materials.[40] The application of these strategies to the architectures here presented for electrochemical flow reactors can be expected.

Friction factor, f_D

The normalized frictional losses across the porous materials were determined using Darcy's friction factor. Figure 8 shows f_D *vs*. mean linear velocity and channel Reynolds number. The usual trend of frictional losses decreasing with rising flow rate is observed. The highest friction factors were 2,113 and 2,436 at 3.1 cm s⁻¹ and 4 cm s⁻¹, respectively, for the circular 10 ppi and 20 ppi materials. Their values of f_D dropped down to 897 and 1,413, respectively, at 13.6 cm s⁻¹. The 20 ppi rectangular and 20 ppi hexagonal specimens displayed approximately the same values over the whole range of mean linear flow velocity. Meanwhile, the lowest values were produced by the triangular pore shape, reaching a minimum 854.6 at 22 cm s⁻¹ for the 10 ppi porosity grade. These values are similar to those reported for Pt/Ti mesh and micromesh, 375 to 12.6 and 3,399 to 173, respectively in a rectangular channel flow cell.[73] Still, they were considerably lower than values achieved with a Pt/Ti felt, which reached a maximum value of 78,157, having pore sizes in the order of micrometers.[73] When compared to porous electrodes in the FM01-L reactor, the 3D printed materials are intermediate between the values for stacked nets and metal foams.[50]

Darcy's permeability, K_D

Darcy's permeability was also calculated based on the pressure drop readings. This coefficient is independent of the viscosity of the fluid and density, therefore, K_D of porous electrodes determined in different liquids (or electrolytes) can be compared. Figure 9 shows the permeability of the 3D printed materials against the mean linear flow rate and Reynolds number. The permeability values displayed slight deviations as the flow rate velocity increased, a behaviour also noted in compressed aluminium foam.[68] This could be explained by the anisotropy found in the 3D printed

structures and the compressed foams, see top and side views of Figure 2. In contrast, for uniform porous electrodes in a rectangular channel flow cell, permeability values were constant over the evaluated range of mean linear flow velocity.[73]

The average values of Darcy's permeability for each porous architecture are listed in Table 5 in increasing order. The 3D printed structure with circular pores, grade 20 ppi is the least permeable, and therefore not the best option in terms of increasing the efficiency of an electrochemical reactor. It is followed by the 30 ppi rectangular electrode. Interestingly, the 10 ppi rectangular and 10 ppi rectangular (2 mm pore size) specimens as well as the 20 ppi rectangular and 20 ppi rectangular (1 mm pore size) specimens show very close values for all the evaluated mean linear flow velocities. One could argue that, in these cases, the size of the pores affects the permeability coefficient to a greater extent than their shape. Therefore, it could be stated that the electrodes with rectangular and hexagonal pores could be used interchangeably. However, when considering its greater volumetric surface area, see Table 3, the rectangular 20 ppi material should be chosen for an electrochemical application over the hexagonal equivalent.

Triangular porous structures are the most permeable, having higher K_D values than those of the other geometrical shapes for both 10 ppi and 20 ppi materials; see Table 5. Moreover, the 10 ppi triangular 3D printed material also produced the lowest pressure gradient and frictional losses. This means that, as a flow-through or flow-across porous electrode, it would require the least electrolyte pumping power among the specimens evaluated in this study (as long as the same flow direction relative to the structure is kept). This is seen more clearly in a plot of K_D vs. A_e (as given

by CAD). Such relationships, shown in Figure 10a) for all the evaluated porous architectures, indicate the ideal trade-off between electrode surface area and hydraulic permeability, i.e. resistance to the fluid flow of an electrolyte. (The same plot taking the A_e values estimated from uncalibrated CT can be seen in Figure S8 in the Supplementary Material. In it, the triangular architectures also perform better the other pore geometries.)

Continuing with Figure 10, the A_e of the CAD 10 ppi triangular specimen was between approximately 1.2 and 1.7 times larger than the surface areas of the electrodes of the same grade but different geometries; see Table 3. It also has close to 25% less mass; see Table 2. This could be a beneficial factor in terms of minimizing the net size, mass and cost of the electrochemical reactor. Furthermore, the 20 ppi triangular specimen has about twice the A_e of its 10 ppi grade equivalent, being also approximately 30% superior to the rectangular and hexagonal geometries. This, suggests that the 20 ppi triangular structure could be advantageous as a porous electrode in an electrochemical flow reactor, having the best combination of high permeability and high surface area among the materials designed in this work. A plot of K_D vs. A_{sv}, seen in Figure 10b), shows essentially the same trends.

These K_D values of the 3D printed porous materials can be put in perspective when compared to those reported in the literature; see Table 6. K_D decreases with decreasing pore diameter of open-cell foams.[75] The reason for this is that for decreasing pore diameter there are more struts in the same volume which obstructs fluid flow.[39] Materials with similar volumetric porosity display close values. Among those previously reported, porous SiC-Al$_2$O$_3$ ($\varepsilon = 0.85$)[39] and alumina foams ($\varepsilon =$

0.80)[55] have permeability values of 5.1×10^{-5} cm^2 and 6.2×10^{-5} cm^2, respectively, being close to the triangular 10 ppi design. Meanwhile, 0.70 porous aluminium foam has a permeability of 1.2×10^{-5} cm^2,[76] being quite close to the 20 ppi hexagonal and rectangular pore architectures. Additionally, the latter is just under the 1.7×10^{-5} cm^2 values reported for Pt/Ti micromesh electrodes.[73] As expected, the permeabilities of materials having significantly larger volumetric porosity or much larger pore sizes are at least one order of magnitude higher than the values presented in the current work. This is the case of aluminium foams with a porosity of 0.92 (108.9×10^{-5} cm^2),[68] and expanded metal mesh (71.0×10^{-5} cm^2).[73] The opposite is true for materials with very small pores, such as carbon felt (0.2×10^{-5} cm^2), or titanium felt (0.1×10^{-5} cm^2), which are less permeable than the circular 20 ppi geometry. In summary, the 3D printed porous architectures display a wide range of hydrodynamic permeability and can be made analogous to conventional porous materials.

Conclusions

- Structures with triangular pores were found to be superior to other architectures considered in this work in terms of suitability for specialized electrochemical cells and reactors as flow-through or flow-across electrodes. The triangular architectures displayed higher permeability, lower mass and increased surface area. These characteristics will diminish electrolyte pumping power, increase the limiting current and mass transfer of the electrochemical reaction and reduce cost and time of manufacture. Improvements of open-cell materials for electrodes can be expected by further topology optimization, tailoring anisotropy and by control of current and potential distribution.

- CT revealed irregularities in the 3D printed materials due to laser movement tolerances, although this could be avoided with the optimization of printing parameters. Volumetric porosity values obtained from CT corresponded to the ones calculated from the measured mass and volume of the specimens. On the other hand, CT surface area estimations turned out to be between 10% and 36% higher than the CAD surface areas. However, our results indicate the importance of surface area metrology in 3D printed porous materials for better accuracy in these estimations.

Acknowledgements

References

1. Lee C-Y, Taylor AC, Nattestad A, Beirne S, Wallace GG. 3D printing for electrocatalytic applications. *Joule* 3(8):1835–49 (2019).

2. Ambrosi A, Shi RRS, Webster RD. 3D-printing for electrolytic processes and electrochemical flow systems. *J Mater Chem A* 8, 21902–21929 (2020).

3. Arenas LF, Ponce de León C, Walsh FC. 3D-printed porous electrodes for advanced electrochemical flow reactors: A Ni/stainless steel electrode and its mass transport characteristics. *Electrochem Commun* 77:133–7 (2017).

4.   Tai XY, Zhakeyev A, Wang H, Jiao K, Zhang H, Xuan J. Accelerating fuel cell development with additive manufacturing technologies: State of the art, opportunities and challenges. *Fuel Cells* 19(6):636–50 (2019).

5.   Arenas LF, Walsh FC, Ponce de León C. 3D-printing of redox flow batteries for energy storage: A rapid prototype laboratory cell. *ECS J Solid State Sci Technol* 4(4):P3080–5 (2015).

6.   Márquez-Montes RA, Collins-Martínez VH, Pérez-Reyes I, Chávez-Flores D, Graeve OA, Ramos-Sánchez VH. Electrochemical engineering assessment of a novel 3D-printed filter-press electrochemical reactor for multipurpose laboratory applications. *ACS Sustainable Chem Eng* 8:3896−3905 (2020).

7.   Ambrosi A, Pumera MP. Multimaterial 3D-printed water electrolyzer with earth-abundant electrodeposited catalysts. *ACS Sustainable Chem Eng* 6:16968–75 (2018).

8.   Walsh FC, Arenas LF, Ponce de León C. Developments in plane parallel flow channel cells. *Curr Opin Electrochem* 16:10–8 (2019).

9.   Walsh FC, Arenas LF, Ponce de León C. A virtuous cycle in materials engineering and surface finishing: Design-print-image. *Trans IMF* 98(2):65–72 (2020).

10.   Tian X, Zhou K. 3D printing of cellular materials for advanced electrochemical energy storage and conversion. *Nanoscale* 12(14):7416–32 (2020).

11.   Egorov V, O'Dwyer C. Architected porous metals in electrochemical energy storage. *Curr Opin Electrochem* 21:201–8 (2020).

12.   Abrantes LM, Three-Dimensional Electrode, in *Encyclopedia of Applied Electrochemistry* ed by Kreysa G, Ota K-I, Savinell RF. Springer, New York, pp 2077–81 (2014).

13.   Couper AM, Pletcher D, Walsh FC. Electrode materials for electrosynthesis. *Chem Rev* 90(5):837–65 (1990).

14.   Walsh FC, Arenas LF, Ponce de León C. Developments in electrode design: structure, decoration and applications of electrodes for electrochemical technology. *J Chem Technol Biotechnol* 93:3073–90 (2018).

15.   Arenas LF, Ponce de León C, Walsh FC. Three-dimensional porous metal electrodes: fabrication, characterisation and use. *Curr Opin Electrochem* 16:1–9 (2019).

16.   Szpyrkowicz L. Application of electrochemical oxidation for treatment of industrial wastewater — the influence of reactor hydrodynamics on direct and mediated processes. J *Chem Technol Biotechnol* 81(8):1375–83 (2006).

17.   Anglada A, Urtiaga A, Ortiz I. Contributions of electrochemical oxidation to waste-water treatment: fundamentals and review of applications. *J Chem Technol Biotechnol* 84(12):1747–55 (2009).

18. Pletcher D. Organic electrosynthesis – A road to greater application. A mini review. *Electrochem Commun* 88:1–4 (2018).

19. Llanos J, Moraleda I, Sáez C, Rodrigo MA, Cañizares P. Reactor design as a critical input in the electrochemical production of peroxoacetic acid. *J Chem Technol Biotechnol* 94(9):2955–60 (2019).

20. Soloman PA, Basha CA, Velan M, Balasubramanian N. Electrochemical degradation of pulp and paper industry waste-water. *J Chem Technol Biotechnol* 84(9):1303–13 (2009).

21. González Pérez O, Castro Larragoitia S, Rodríguez-Torres I. Preliminary studies on the electrochemical recovery of Zn and Cd from effluent produced by a zinc refinery plant using a filterpress reactor. *J Chem Technol Biotechnol* 88(7):1371–9 (2012).

22. Sánchez-Díez E, Ventosa E, Guarnieri M, Trovò A, Flox C, Marcilla R, et al. Redox flow batteries: Status and perspective towards sustainable stationary energy storage. *J Power Sources* 481:228804 (2021).

23. Zhang Y-Z, Wang Y, Cheng T, Yao L-Q, Li X, Lai W-Y, et al. Printed supercapacitors: materials, printing and applications. *Chem Soc Rev* 48(12):3229–64 (2019).

24. Gu DD, Meiners W, Wissenbach K, Poprawe R. Laser additive manufacturing of metallic components: materials, processes and mechanisms. *Int Mater Rev* 57(3):133–64 (2012).

25. Lee C-Y, Taylor AC, Beirne S, Wallace GG. 3D-Printed conical arrays of TiO_2 electrodes for enhanced photoelectrochemical water splitting. *Adv Energy Mater* 7(21):1701060 (2017).

26. Arenas LF, Kaishubayeva N, Ponce de León C, Walsh FC. Electrodeposition of platinum on 3D-printed titanium mesh to produce tailored, high area anodes. *Trans IMF* 98(1):48–52 (2020).

27. Lölsberg J, Starck O, Stiefel S, Hereijgers J, Breugelmans T, M W. 3D-Printed electrodes with improved mass transport properties. *ChemElectroChem* 4(12):3309–13 (2017).

28. Hereijgers J, Schalck J, Lölsberg J, Wessling M, Breugelmans T. Indirect 3D printed electrode mixers. *ChemElectroChem* 6(2):378–82 (2019).

29. Cheng TS, Nasir MZM, Ambrosi A, Pumera M. 3D-printed metal electrodes for electrochemical detection of phenols. *Appl Mater Today* 9:212–9 (2017).

30. Huang X, Chang S, Lee WSV, Ding J, Xue JM. Three-dimensional printed cellular stainless steel as a high-activity catalytic electrode for oxygen evolution. *J Mater Chem A* 5(34):18176–82 (2017).

31. Arenas LF, Boardman RP, Ponce de León C, Walsh FC. X-ray computed micro-tomography of reticulated vitreous carbon. *Carbon* 135:85–94 (2018).

32. Catañeda LF, Rivera FF, Pérez T, Nava JL. Mathematical modeling and simulation of the reaction environment in electrochemical reactors. *Curr Opin Electrochem* 16:75–82 (2019).

33. Trasatti S, Petrii OA. Real surface area measurements in electrochemistry. *Pure Appl Chem* 63(5):711–34 (1991).

34. Langlois S, Coeuret F. Flow-through and flow-by porous electrodes of nickel foam. II. Diffusion-convective mass transfer between the electrolyte and the foam. *J Appl Electrochem* 19(1):51–60 (1989).

35. Jervis R, Kok MDR, Neville TP, Meyer Q, Brown LD, Iacoviello F, et al. In situ compression and X-ray computed tomography of flow battery electrodes. *J Energy Chem* 27(5):1353–61 (2018).

36. Olvera OG, Lapidus-Lavine GT. Use of X-ray tomography for the experimental verification of a mathematical model for the recovery of Cu and Cd in a flow-by porous electrode reactor. *Int J Chem React Eng* 10:A36 (2012).

37. Arenas LF, Ponce de León C, Boardman RP, Walsh FC. Electrodeposition of platinum on titanium felt in a rectangular channel flow cell. *J Electrochem Soc* 164(2):D57–D66 (2017).

38. Arenas LF, Ponce de León C, Boardman RP, Walsh FC. Characterisation of platinum electrodeposits on a titanium micromesh stack in a rectangular channel flow cell. *Electrochim Acta* 247:994–1005 (2017).

39. Innocentini MDM, Salvini VR, Macedo A, Pandolfelli VC. Prediction of ceramic foams permeability using Ergun's equation. *Materials Research* 2(4):283–9 (1999).

40. Ou X, Zhang X, Lowe T, Blanc R, Rad MN, Wang Y, et al. X-ray micro computed tomography characterization of cellular SiC foams for their applications in chemical engineering. *Mater Charact* 123:20–8 (2017).

41. Liu X, Li X, Ju S, Gu Y, Tan W, Li X, et al. Miniaturized application of 3D-printed large-flow microreactor in extraction and separation of platinum, palladium, and rhodium. *J Chem Technol Biotechnol* 96:1007–1015 (2021).

42. Brown CJ, Walsh FC, Pletcher D. Mass transfer and pressure drop in a laboratory filterpress electrolyser. *Trans IChemE* 73(A):196–205 (1995).

43. Kim MJ, Seo Y, Cruz MA, Wiley BJ. Metal nanowire felt as a flow-through electrode for high-productivity electrochemistry. *ACS Nano* 13(6):6998-7009 (2019).

44. MacDonald M, Darling RM. Modeling flow distribution and pressure drop in redox flow batteries. *AIChE J* 64(10):3746–55 (2018).

45. Pletcher D, Whyte I, Walsh FC, Millington JP. Reticulated vitreous carbon cathodes for metal ion removal from process streams part I: Mass transport studies. *J Appl Electrochem* 21(8):659–66 (1991).

46. Milshtein JD, Tenny KM, Barton JL, Drake J, Darling RM, Brushett FR. Quantifying mass transfer rates in redox flow batteries. *J Electrochem Soc* 164(11):E3265–75 (2017).

47. Langlois S, Coeuret F. Flow-through and flow-by porous electrodes of nickel foam. I. Material characterization. *J Appl Electrochem* 19(1):43–50 (1989).

48. González-García J, Bonete P, Expósito E, Montiel V, Aldaz A, Torregrosa-Maciá R. Characterization of a carbon felt electrode: structural and physical properties. *J Mater Chem* 9(2):419–26 (1999).

49. Pletcher D, Walsh FC. Three-dimensional electrodes, in *Electrochemistry for a Cleaner Environment,* ed by Genders D, Weinberg N. The Electrosynthesis Company, New York, pp. 51–100 (1992).

50. Brown CJ, Pletcher D, Walsh FC, Hammond JK, Robinson D. Studies of space-averaged mass transport in the FM01-LC laboratory electrolyser. J Appl Electrochem 23(1):38–43 (1993).

51. Rousar I, Cezner V. Mass transfer coefficients and friction coefficients for rough electrodes, in *Institution of Chemical Engineers Symposium Series No. 98*, pp. 85–95 (1986).

52. Müller V, Rousar I. Mass transfer coefficient and pressure losses for membrane cell with spacers, in *Dechema Monographs No. 123*, VCH, Weinhein, pp. 331–45 (1991).

53. Culcasi A, Gurreri L, Zaffora A, Cosenza A, Tamburini A, Micale G. On the modelling of an Acid/Base Flow Battery: An innovative electrical energy storage device based on pH and salinity gradients. *Appl Energy* 277:115576 (2020).

54. Aparicio-Mauricio G, Rodríguez FA, Pijpers JJH, Cruz-Díaz MR, Rivero EP. CFD modeling of residence time distribution and experimental validation in a redox flow battery using free and porous flow. *J Energy Storage* 29:101337 (2020).

55. Incera Garrido G, Patcas FC, Lang S, Kraushaar-Czarnetzki B. Mass transfer and pressure drop in ceramic foams: A description for different pore sizes and porosities. *Chem Eng Sci* 63(21):5202–17 (2008).

56. Averbukh M, Pozin A, Sukoriansky S. Electrolyte pumping optimization in already manufactured vanadium redox battery based on experimentally determined electrical and hydrodynamic losses. *J Energy Eng* 143(2):04016050 (2017).

57. Forner-Cuenca A, Penn EE, Oliveira AM, Brushett FR. Exploring the role of electrode microstructure on the performance of non-aqueous redox flow batteries. *J Electrochem Soc* 166(10):A2230–41 (2019).

58. Bracconi M, Ambrosetti M, Okafor O, Sans V, Zhang X, Ou X, et al. Investigation of pressure drop in 3D replicated open-cell foams: Coupling CFD with experimental data on additively manufactured foams. *Chem Eng J* 377:120123 (2019).

59. Yamashin Steel Co. Inc., Specific gravity (density) of stainless steel, etc. (2015). http://www.yamco-yamashin.com/en/products/guide_specific_gravity.html.

60. Cengel YA, Cimbala JM. *Fluid Mechanics. Fundamentals and Applications.* McGraw-Hill Higher Education, London (2010).

61. Jorné J, Roayaie E. Effect of pore-size distribution on metal ion removal in flow-through porous electrodes. *J Electrochem Soc* 133(8):1649–53 (1986).

62. Walsh FC, Arenas LF, Ponce de León C, Reade GW, Whyte I, Mellor BG. The continued development of reticulated vitreous carbon as a versatile electrode material: Structure, properties and applications. *Electrochim Acta* 215:566–91 (2016).

63. Kruth J-P, Bartscher M, Carmignato S, Schmitt R, De Chiffre L, Weckenmann A. Computed tomography for dimensional metrology. *CIRP Annals* 60(2):821–42 (2011).

64. Kiekens K, Welkenhuyzen F, Tan Y, Bleys P, Voet A, Kruth J-P, et al. A test object with parallel grooves for calibration and accuracy assessment of industrial computed tomography (CT) metrology. *Meas Sci Technol* 22(11):115502 (2011).

65. Friedrich JM, Ponce de León C, Reade GW, Walsh FC. Reticulated vitreous carbon as an electrode material. *J Electroanal Chem* 561(1-2):203–17 (2004).

66. Bruns S, Stipp SLS, Sørensen HO. Statistical representative elementary volumes of porous media determined using greyscale analysis of 3D tomograms. *Adv Water Resour* 107:32–42 (2017).

67. Pletcher D, Whyte I, Walsh FC, Millington JP. Reticulated vitreous carbon cathodes for metal ion removal from process streams part II: Removal of copper(II) from acid sulphate media. *J Appl Electrochem* 21(8):667–71 (1991).

68. Boomsma K, Poulikakos D. The effects of compression and pore size variations on the liquid flow characteristics in metal foams. *J Hydroinform* 124:263–72 (2002).

69. Inayat A, Schwerdtfeger J, Freund H, Körner C, Singer RF, Schwieger W. Periodic open-cell foams: Pressure drop measurements and modeling of an ideal tetrakaidecahedra packing. *Chem Eng Sci* 66(12):2758–63 (2011).

70. Castañeda LF, Walsh FC, Nava JL, Ponce de León C. Graphite felt as a versatile electrode material: Properties, reaction environment, performance and applications. *Electrochim Acta* 258:1115–39 (2017).

71. González-García J, Montiel V, Aldaz A, Conesa JA, Pérez JR, Codina G. Hydrodynamic behavior of a filter-press electrochemical reactor with carbon felt as a three-dimensional electrode. *Ind Eng Chem Res* 37(11):4501–11 (1998).

72. Montillet A, Comiti J, Legrand J. Application of metallic foams in electrochemical reactors of filter-press type part I: flow characterization. *J Appl Electrochem* 23(10):1045–50 (1993).

73. Arenas LF, Ponce de León C, Walsh FC. Pressure drop through platinized titanium porous electrodes for cerium-based redox flow batteries. *AIChE J* 64(3):1135–46 (2018).

74. Colli AN, Toelzer R, Bergmann MEH, Bisang JM. Mass-transfer studies in an electrochemical reactor with a small interelectrode gap. *Electrochim Acta* 100:78–84 (2013).

75. Khayargoli P, Loya V, Lefebvre LP, Medraj M. The impact of microstructure on the permeability of metal foams, in *Proceedings of the 2004 Canadian Society of Mechanical Engineering*, CSME forum 2004, London (Canada), pp. 221–228 (2004).

76. Miwa S, Revankar ST. Hydrodynamic characterization of nickel metal foam, Part 1: Single-phase permeability. *Transp Porous Med* 80(2):269–79 (2009).

77. Antohe BV, Lage JL, Price DC, Weber RM. Experimental determination of permeability and inertia coefficients of mechanically compressed aluminum porous matrices. *J Fluids Eng* 119(2):404–12 (1997).

Tables

Table 1. Nominal dimensions, volumetric porosity, surface area and linear porosity grade of the porous architectures, according to the CAD suite. Digital objects are cylinders of 30 mm diameter, 20 mm in height.

Electrode material	Primary pore size / mm	Secondary pore size / mm	Distance between pores in 3 dimensions / mm			Solid volume / cm^3	Void volume / cm^3	Surface area, A / cm^2	Volumetric porosity, ε	Porosity grade / ppi
			x	y	z					
Rectangular 10 ppi	2.00	2.00	0.62	0.62	0.62	3.58	10.56	201.59	0.75	10.00
Rectangular 20 ppi	1.00	1.00	0.31	0.31	0.31	3.58	10.56	403.11	0.75	19.99
Rectangular 30 ppi	0.70	0.70	0.17	0.17	0.17	2.51	11.63	541.98	0.82	30.08
Circular 10 ppi	2.00	2.60	0.62	0.62	0.62	3.62	10.52	261.09	0.74	10.00
Circular 20 ppi	1.00	1.30	0.31	0.31	0.31	3.59	10.55	512.03	0.75	19.99
Hexagonal 10 ppi	2.00	2.00	0.62	0.62	0.62	3.58	10.56	200.53	0.75	10.00
Hexagonal 20 ppi	1.00	1.00	0.31	0.31	0.31	3.61	10.53	403.04	0.74	19.99
Triangular 10 ppi	2.00	2.00	0.62	0.62	0.62	2.92	11.22	313.98	0.79	10.00
Triangular 20 ppi	1.00	1.00	0.31	0.31	0.31	2.97	11.17	628.96	0.79	19.99

Table 2. Measured dimensions and mass of 3D printed specimens of the porous architectures along a comparison of the calculated and CT-determined porosity and surface area *vs*. nominal CAD values.

Electrode material	Mass / g	Diameter / mm	Height / mm	Volumetric porosity, ε					Surface area, A / cm^2		
				CAD	CT	Mass	CT *vs*. CAD % difference	Mass *vs*. CAD % difference	CAD	CT	CT *vs*. CAD % difference
Rectangular 10 ppi	33.75	29.97	20.00	0.75	-	0.70	-	-6.7	201.59	-	-
Rectangular 20 ppi	37.46	30.24	19.61	0.75	0.64	0.67	-14.7	-10.7	403.11	541.31	+34.3
Rectangular 30 ppi	49.06	30.16	19.95	0.82	0.55	0.57	-32.9	-30.5	541.98	851.87	+57.2
Circular 10 ppi	34.27	30.06	19.62	0.74	-	0.69	-	-6.8	261.09	-	
Circular 20 ppi	47.80	30.04	19.83	0.75	0.57	0.57	-24.0	-24.0	512.03	566.49	+10.6
Hexagonal 10 ppi	34.15	30.10	20.14	0.75	-	0.70	-	-6.7	200.53	-	-
Hexagonal 20 ppi	39.54	30.41	19.96	0.74	0.65	0.66	-12.2	-10.8	403.04	539.65	+33.9
Triangular 10 ppi	26.82	30.09	19.54	0.79	0.74	0.76	-6.3	-3.8	313.98	366.82	+16.8
Triangular 20 ppi	38.61	30.03	19.69	0.79	0.64	0.65	-19.0	-17.7	628.96	727.92	+15.7

Table 3. Calculated volumetric surface area and surface are per unit solid volume of 3D printed specimens of the porous electrode architectures from CT scans *vs.* nominal CAD values.

Electrode material	Volumetric surface area, A_e / cm^{-1}			Surface area per unit solid volume, A_{sv} / cm^{-1}		
	CAD	CT	CT *vs.* CAD % difference	CAD	CT	CT *vs.* CAD % difference
Rectangular10 ppi	14.26	-	-	57.04	-	-
Rectangular 20 ppi	28.51	38.43	+34.7	114.06	106.67	-6.5
Rectangular 30 ppi	38.34	59.77	+56.0	212.98	132.89	-37.6
Circular 10 ppi	18.47	-	-	71.03	-	-
Circular 20 ppi	36.22	40.31	+11.3	144.87	93.72	-35.3
Hexagonal 10 ppi	14.18	-	-	56.74	-	-
Hexagonal 20 ppi	28.51	37.22	+30.5	109.65	106.29	-3.1
Triangular 10 ppi	22.21	26.40	+18.9	105.76	101.54	-4.0
Triangular 20 ppi	44.49	52.20	+17.3	211.86	145.00	-31.6

Table 4. Empirical coefficients *e* and *h* for the relationship between ΔP and Reynolds number ($\Delta P = e\,Re^{h}$) for the 3D printed porous electrode materials along comparative data for some conventional flow-through electrodes for electrochemical reactors including examples of planar electrodes plus a turbulence promoter (polymer mesh).

Electrode material	*e* / Pa	*h*	Source
Rectangular 10 ppi	1.53×10^{-2}	1.28	This work
Rectangular 20 ppi	4.72×10^{-2}	1.27	This work
Rectangular 30 ppi	3.04×10^{-2}	1.47	This work
Circular 10 ppi	3.52×10^{-2}	1.41	This work
Circular 20 ppi	1.57×10^{-2}	1.57	This work
Hexagonal 10 ppi	0.94×10^{-2}	1.33	This work
Hexagonal 20 ppi	0.61×10^{-2}	1.51	This work
Triangular 10 ppi	2.66×10^{-2}	1.16	This work
Triangular 20 ppi	3.12×10^{-2}	1.24	This work
Ni plate (unrestricted channel)	2.0×10^{-2}	1.29	[74]
Ni plate (promoter EPM2)	4.1×10^{-2}	1.61	[74]
Pt/Ti micromesh	114.6	1.07	[73]
Pt/Ti plate (promoter mesh)	10.1	0.82	[73]
Pt/Ti mesh	9.2	0.61	[73]
FM01-LC Cu plate (promoter E)	0.31	1.42	[50]
FM01-LC Cu plate (promoter F)	0.30	1.33	[50]

Table 5. Calculated Darcy's permeability of the evaluated porous electrodes, listed in increasing order. The porosity of 3D printed specimens is based on their mass.

Electrode material	Volumetric porosity (from mass), ε	K_D / 10^{-5} cm^2
Circular 20 ppi	0.57	0.35
Rectangular 30 ppi	0.57	0.53
Circular 10 ppi	0.69	0.61
Rectangular 20 ppi	0.67	1.15
Hexagonal 20 ppi	0.66	1.28
Triangular 20 ppi	0.65	2.31
Rectangular 10 ppi	0.70	3.42
Hexagonal 10 ppi	0.70	3.83
Triangular 10 ppi	0.76	5.37

Table 6. Permeability coefficients of various porous materials and porous electrodes.

Material	Porosity grade / ppi	Volumetric porosity, ε	K_D / 10^{-5} cm^2	Source
SiC-Al$_2$O$_3$ foam	45	0.88	25.6	[39]
	60	0.85	5.1	[39]
Al$_2$O$_3$ foam	45	0.80	6.23	[55]
	45	0.85	9.95	[55]
Al foam	N/A	0.30	0.1	[77]
	N/A	0.70	1.2	[77]
	10	0.92	352.9	[68]
	20	0.92	108.9	[68]
	40	0.93	70.2	[68]
Ni foam	45	0.97	21.4	[34]
	60	0.97	8.23	[34]
	60	0.90	21.2	[76]
	100	0.97	3.15	[34]
Carbon felt	N/A	0.96	0.24	[56]
Pt/Ti felt	N/A	0.80	0.13	[73]
Pt/Ti mesh	N/A	0.71	71.0	[73]
Pt/Ti micromesh	N/A	0.53	1.67	[73]
Pt/Ti plate + TP	N/A	0.78	44.5	[73]

Figures
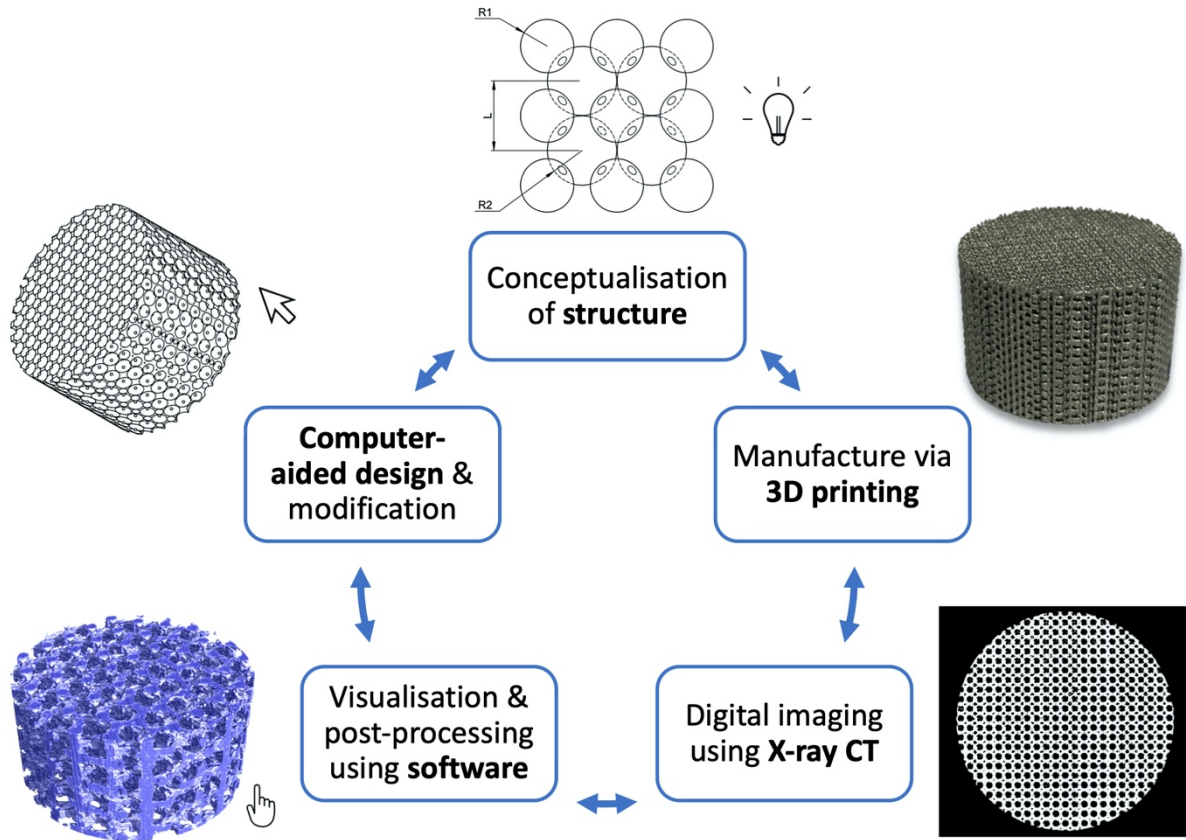
Figure 1. 'Virtuous cycle' for an iterative process involving digital design, manufacture and imaging during the development and production of 3D printed porous electrode architectures for electrochemical flow reactors and other electrochemical devices.[8,9]
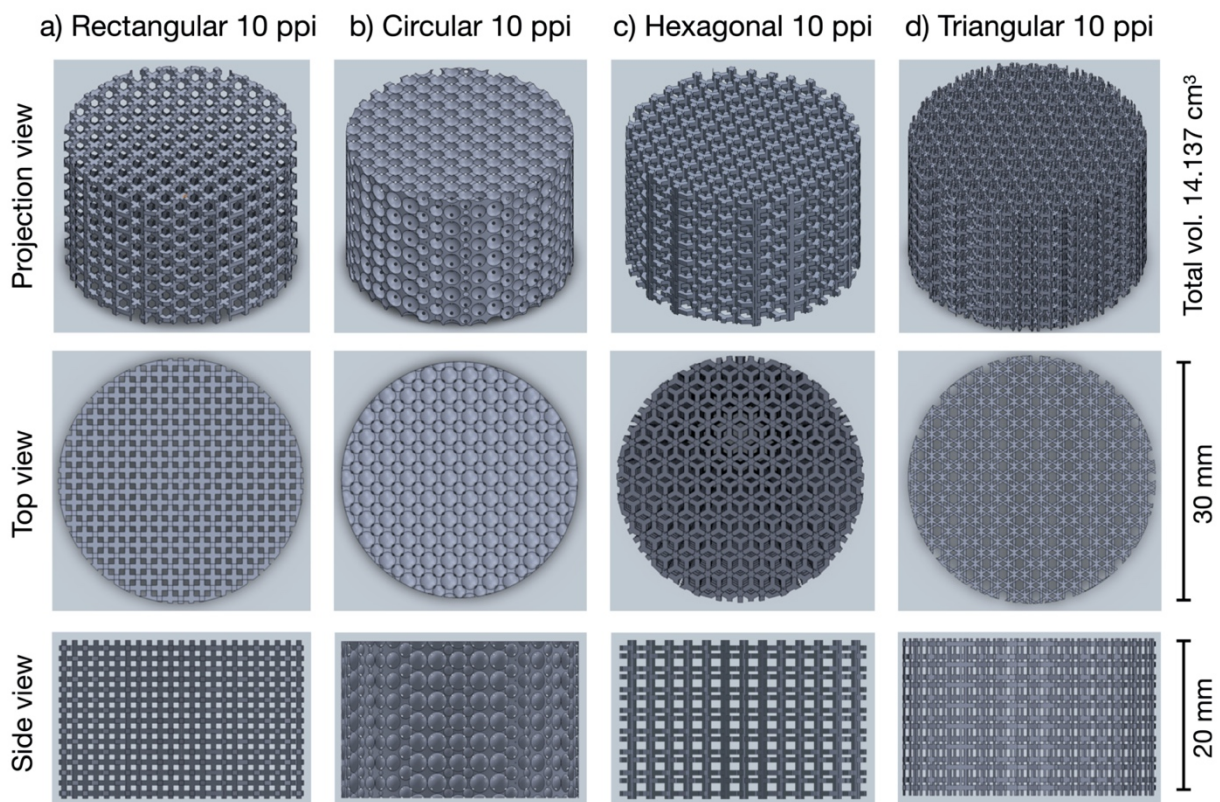
Figure 2. Isometric, top and side views of CAD-designed porous electrode architectures. For clarity, only the 10 ppi porosity grade of each pore shape is shown here.
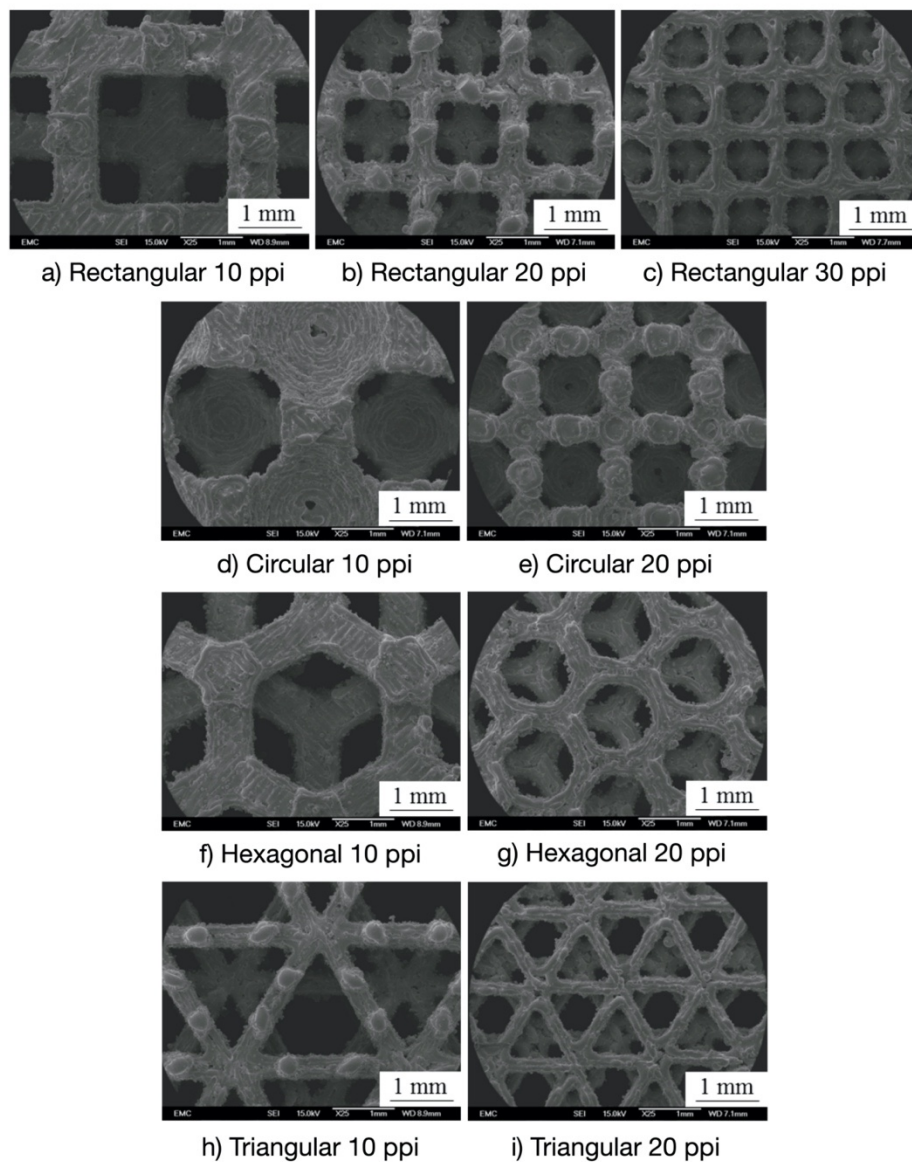
Figure 3. SEM images of 3D printed specimens of the different porous electrode architectures. Magnification 25x.
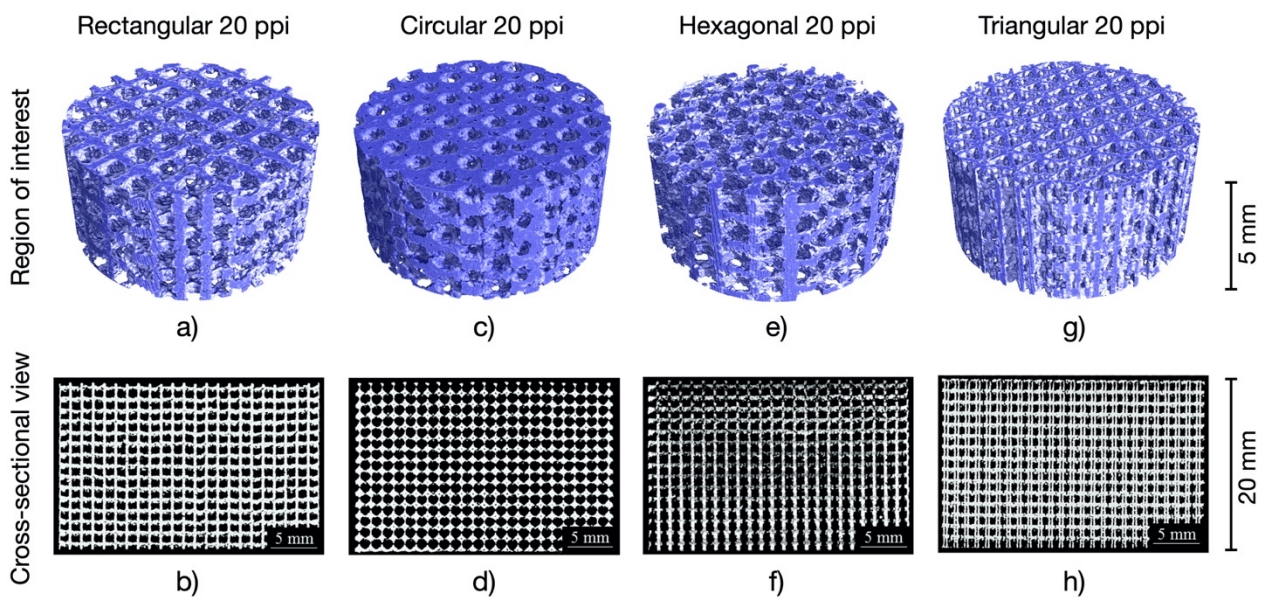
Figure 4. CT images of 3D printed specimens of the porous electrode architectures. For clarity, only the 20 ppi porosity grade of each pore shape is shown here. a), c), e) and g) Three-dimensional regions of interest (ROI) with a diameter of 10 mm and a height of 5 mm within the full specimens. b), d), f) and h) Cross-sectional views of the full specimens (30 mm diameter and 20 mm height).
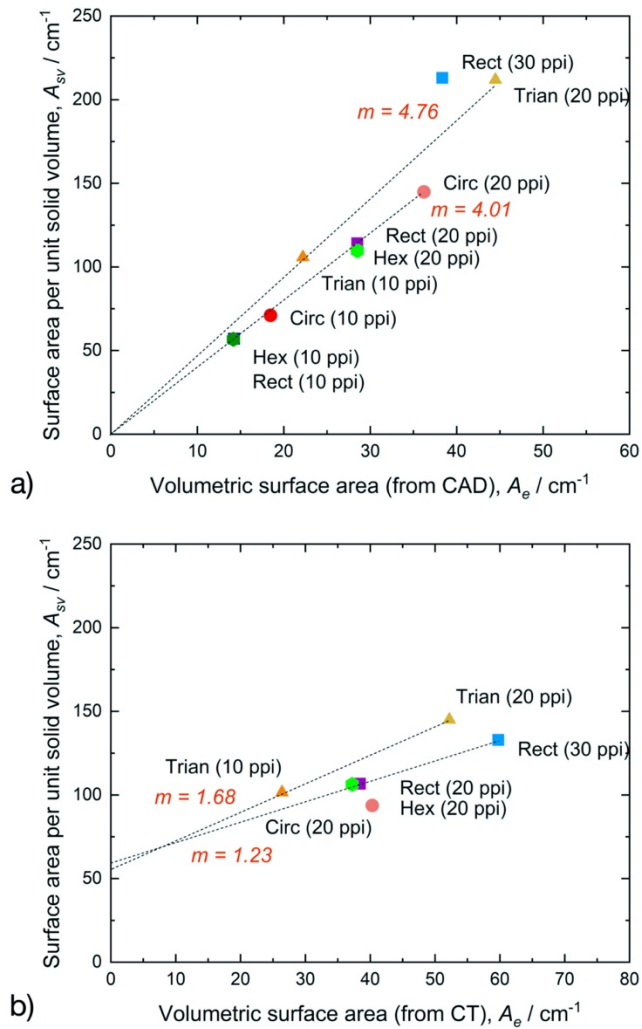
Figure 5. Plot of volumetric surface area *vs*. surface area per unit solid volume for different porous electrode architectures. a) From nominal CAD dimensions. b) From CT scans with a resolution of 0.0187 mm per voxel and ISO50% thresholding.
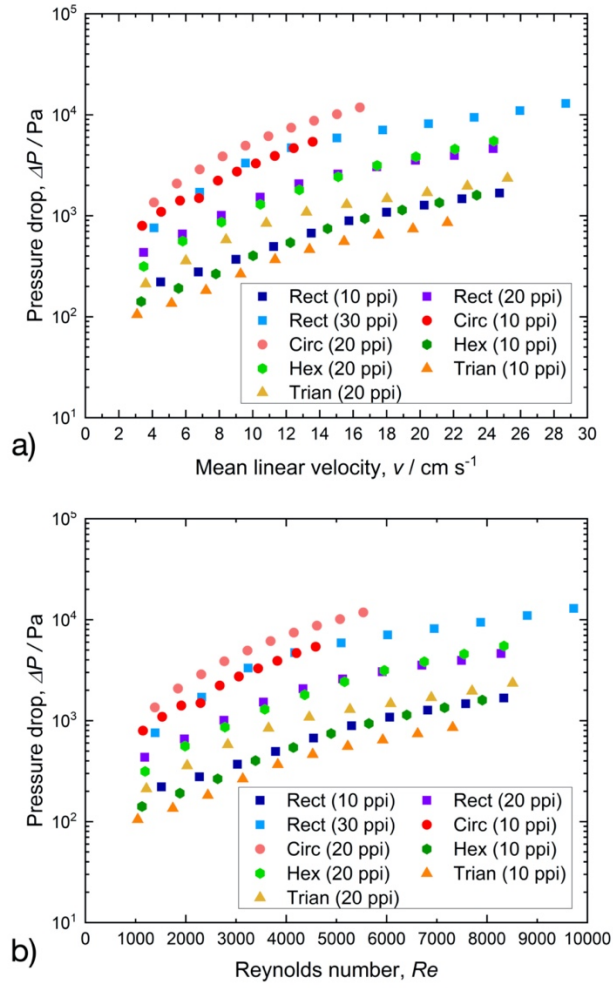
Figure 6. Pressure drop *vs*. mean linear flow velocity and Reynolds number measured across different porous electrode architectures. Flow path length: 20 mm.
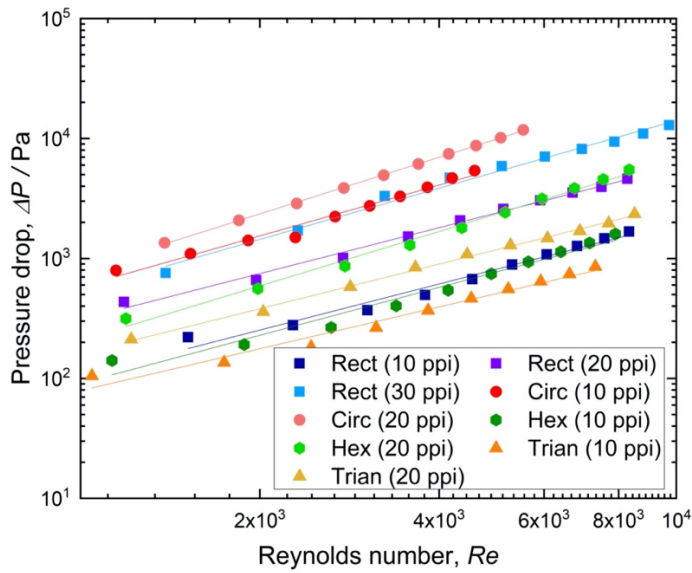
Figure 7. Pressure drop (logarithmic scale) *vs.* Reynolds number (logarithmic scale) measured across different porous electrode architectures. Flow path length: 20 mm.
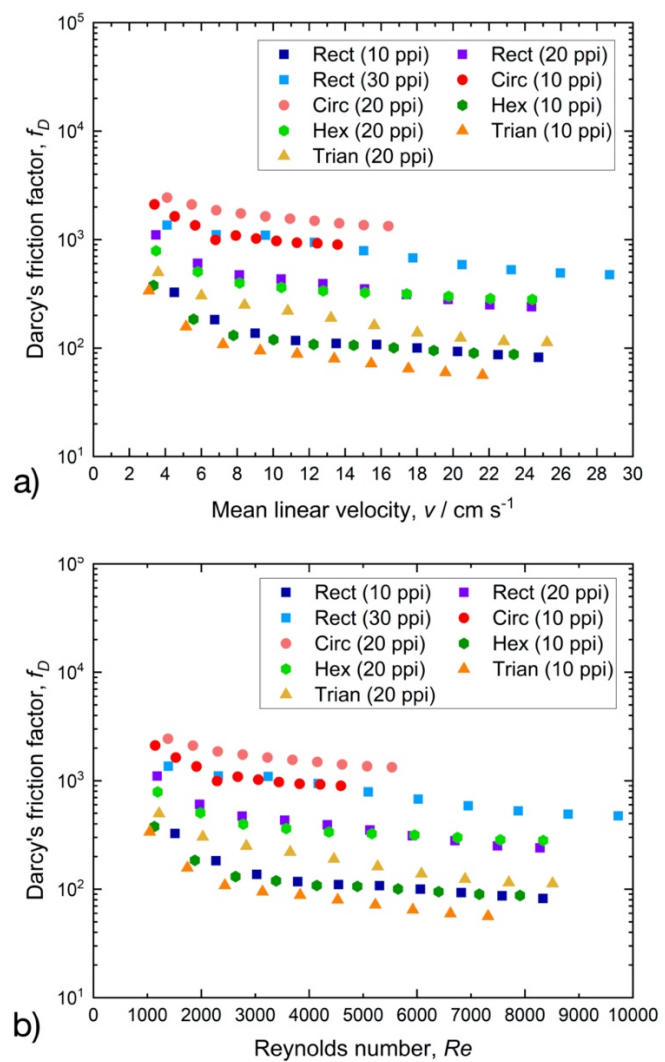
Figure 8. Darcy's friction factor *vs*. mean linear flow velocity and Reynolds number for different porous electrode architectures.
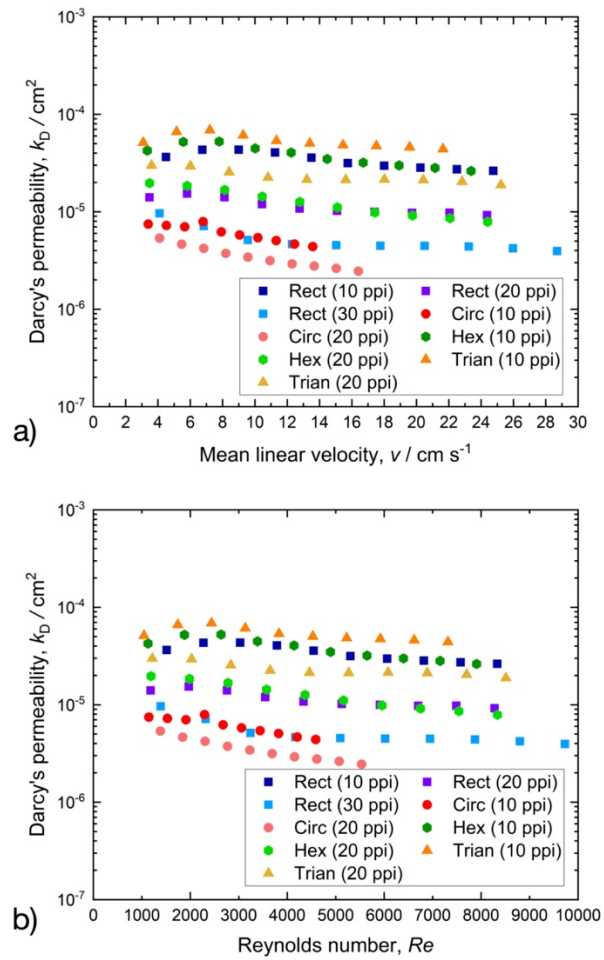
Figure 9. Darcy's permeability *vs.* mean linear flow velocity and Reynolds number for different porous electrode architectures.
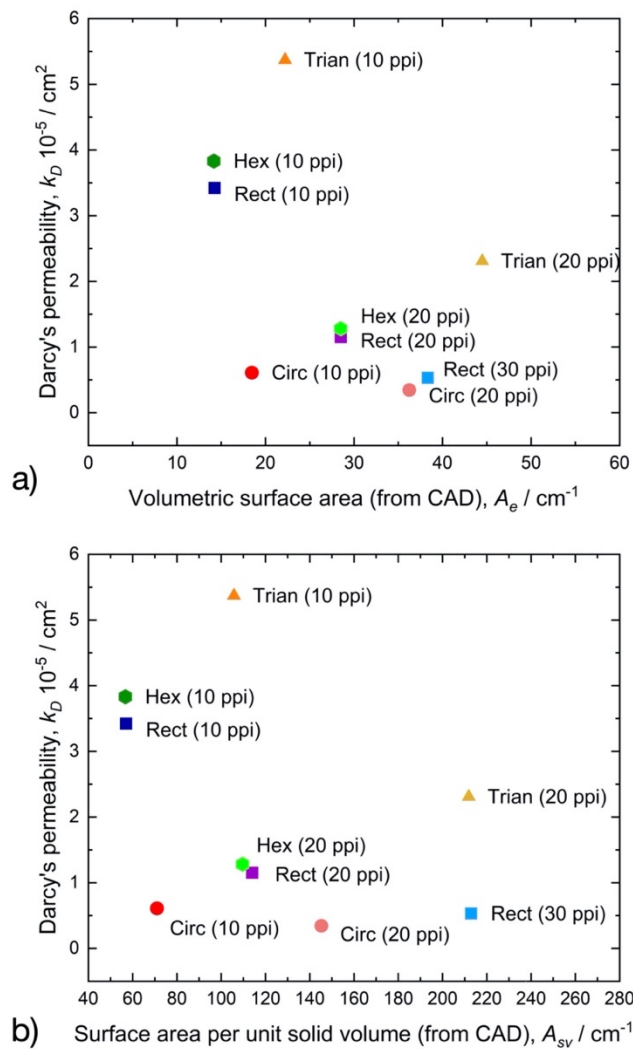
Figure 10. Relationship between hydraulic and surface area properties for different porous electrode architectures. Surface area taken from CAD dimensions. a) Darcy's permeability *vs*. volumetric surface area. b) Darcy's permeability *vs*. surface area per unit solid volume.